Nanoscale

PAPER

View Article Online
View Journal | View Issue

Cite this: *Nanoscale*, 2019, **11**, 11782

Plasmon-induced hot electron transfer in Au–ZnO heterogeneous nanorods for enhanced SERS†

Jun Zhou,[a,b] Jianshuo Zhang,‡[b] Haitao Yang, *[b] Zhuan Wang, *[b] Jin-an Shi,[c] Wu Zhou,[c] Nan Jiang, [d] Guoyu Xian,[b] Qi Qi,[b] Yuxiang Weng,[b] Chengmin Shen,[b] Zhaohua Cheng[b] and Shengtai He *[a]

Received 7th April 2019,
Accepted 23rd May 2019

DOI: 10.1039/c9nr02969a

rsc.li/nanoscale

Colloid-synthesized matchstick-shaped Au–ZnO heterogeneous nanorods are found to have the Zn ion terminated plane in the ZnO–Au interface without the formation of Au–O bonds based on the atomic-resolution observation of their interfacial structure and electronic states, which is greatly different from the other reported results. The Au–ZnO heterogeneous nanorods with a good expitaxial interface have shown a stronger surface-enhanced Raman scattering (SERS) signal of the dopamine molecules than Au nanoscale seeds alone, which is attributed to the enhanced charge transfer (CT) effect of ZnO which is greatly improved by the plasmon-induced hot electron from Au nanostructures. The enhanced CT effect has also been proved by a higher photocatalysis efficiency. Furthermore, the plasmon-induced hot electron transfer mechanism in Au–ZnO heterogeneous nanorods has been confirmed by a slow rise time of electrons in the transient absorption measurements. These findings suggest the dependency of the plasmon-induced hot electron transfer mechanism on the different mixing of the metal and semiconductor band levels.

Introduction

Metal–semiconductor heterogeneous nanorods (NRs) can greatly enhance and trap light mainly by scattering photons, plasmon resonance energy transfer, and plasmon-induced hot electrons from metal nanostructures.[1,2] Diverse metal–semiconductor heterogeneous nanostructures have recently been of significant interest both in the fundamental light–matter interaction mechanism and technological applications, including photovoltaics, photocatalysis, and spectroscopic applications, particularly in surface-enhanced Raman spectroscopy (SERS),[3–5] on account of the advantages of broad spectral tunability, large absorption cross sections, and long-term stability of plasmonic metal nanostructures. By exploring the chemical enhancement of semiconductor nanostructures along with electromagnetic (EM) enhancement of plasmonic metal nanostructures, many research efforts have been focused on the pursuit of more sensitive SERS-active substrates, possibly extending to the level of single molecule detection sensitivity.[6] Since chemical enhancement is mostly related to the CT between the absorbate molecules and semiconductor,[7,8] the highly-efficient injection of plasmon-induced hot electrons into the semiconductor has become a key problem.

So far, there are two different plasmon-induced hot electron injection mechanisms. One is the plasma-induced hot electron transfer mechanism (PHET), which refers to the transfer of hot electrons formed by the plasmon decay of metal nanostructures into a coupled semiconductor,[9,10] and the other is the plasmon-induced metal-to-semiconductor interfacial charge-transfer transition (PICTT) mechanism, which refers to the direct generation of an electron in the coupled semiconductor and an electron hole in the plasmonic metal in the decay process of plasmons.[11,12] The PICCT mechanism was first reported to have a highly efficient plasmon-induced electron–hole pair separation in Au–CdSe NRs with Au tips at both the ends of CdSe NRs. CdSe is a narrow band gap semiconductor with a band gap of 1.76 eV and the Schottky barrier of Au–CdSe is 0.64 eV. However, there are still few reports on the plasmon-induced hot electron injection mechanism in one dimensional (1D) heterogeneous nanostructures formed by plasmatic metal and wide-band gap semiconductors and its influence on SERS.

---

[a] *School of Material Science and Engineering, Tianjin Polytechnic University, Tianjin 300387, China. E-mail: sht-he@tjpu.edu.cn*

[b] *Beijing National Laboratory for Condensed Matter Physics, Institute of Physics, Chinese Academy of Sciences, Beijing 100190, P. R. China. E-mail: htyang@iphy.ac.cn, zhuanwang@ iphy.ac.cn*

[c] *School of Physics Science, University of Chinese Academy of Sciences, Beijing 100190, P. R. China*

[d] *Department of Chemistry, University of Illinois at Chicago, Chicago, Illinois 60607, USA*

† Electronic supplementary information (ESI) available. See DOI: 10.1039/c9nr02969a

‡ The author contributed equally to this work.

Herein, we propose Au–ZnO 1D plasmonic metal–semiconductor NRs with a Au tip only at one end of ZnO NRs to experimentally demonstrate the enhanced SERS and the PHET mechanism in metal and wide-band gap semiconductor nanostructures. ZnO can epitaxially grow on Au seeds due to a suitable crystalline lattice match between them, resulting in a weakly coupled interface. ZnO also has a good affinity with molecules to realize CT enhanced SERS. The length of the ZnO nanorods is much longer than the diameter of Au seeds, which can ensure a long enough relaxation path of hot electrons. Moreover, since the band gap of ZnO and the Schottky barrier of Au–ZnO, 3.37 eV and 1.2 eV,[13,14] are quite different from the relevant values of CdSe and Au–CdSe, Au–ZnO NRs can be regarded as a typical metal/wide-band gap semiconductor nanostructure for the investigation of enhanced SERS and the plasmon-induced hot electron injection mechanism.

Experiments

Matchstick-shaped Au–ZnO heterogeneous NRs were prepared by a high-temperature solution method. Typically, gold(III) chloride hydrate, benzyl alcohol, 1-octadecene, oleylamine, and zinc acetate dehydrate were added into a three-neck flask and warmed at 120 °C. After the color of the solution changed from yellow to brown, the solution was further heated to 180 °C and incubated for 30 min. The Au–ZnO NRs were collected by centrifugation after cooling the reaction solution to room temperature. Au seeds were obtained by directly extracting a small amount of reaction solution at 120 °C followed by washing with ethanol and re-dispersing with hexane. ZnO NRs were prepared by removing Au tips from Au–ZnO NRs by an etching treatment with KI and iodine. The detailed synthesis information is presented in the ESI.†

Au seeds, ZnO NRs, and Au–ZnO NRs were deposited on the SiO_2/Si substrates for SERS measurements, respectively. A total of 100 μL of hexane dispersion of the hydrophobic nanostructures was added dropwise onto 1×1 cm^2 SiO_2/Si wafer with a 300 nm SiO_2 top layer and dried under ambient conditions. Then, this SiO_2/Si wafer was put into a 5 mL beaker containing 1 mL of 1×10^{-5} M dopamine solution. After 12 hours, SiO_2/Si wafers covered with the different samples were washed three times with ethanol and dried in air.

Characterization

Powder X-ray diffraction (XRD) data were collected on a D2 PHASER X-ray diffractometer (Cu Kα radiation, $\lambda = 0.154$ nm). The morphology and structural properties of the samples were investigated by using a transmission electron microscope (TEM, JEM-2100F with an operation voltage of 200 kV). STEM characterization was performed on an aberration-corrected scanning transmission electron microscope operated at 60 kV. The convergence angle was set to 32 mrad, while the angle of the annular darkfield detector was set to 75–210 mrad to obtain the atomic number contrast (*Z*-contrast) in the images. The samples for STEM analysis were prepared by adding dropwise a hexane solution of Au–ZnO NRs onto TEM grids and drying. UV-visible spectra were recorded with a Varian Cary 5000 ultraviolet-visible spectrophotometer. Raman spectra were obtained with a Renishaw Raman system model in a *Via*-Reflex spectrometer and a LabRam HR 800 spectrometer of HORIBA Co. 532 nm radiation from a solid-state laser, 632.8 nm radiation from a He–Ne laser and 785 nm radiation from a semiconductor-state laser were used as exciting sources. Femtosecond time-resolved mid-IR absorption was carried out with a home-made ultrafast system.

Results and discussion

Fig. 1 shows the transmission electron microscopy (TEM) images of the as-prepared Au seeds, ZnO NRs, and matchstick-shaped Au–ZnO NRs, respectively. From Fig. 1c, it can be observed that the average length and diameter of ZnO NRs are 46.0 nm and 9.0 nm, respectively, while the size of the Au tips (darker parts) is about 8.0 nm and is close to the size of Au seeds. Fig. 1d presents the corresponding high-resolution TEM images indicating highly co-aligned lattices of all Au and ZnO domains from epitaxial growth of the ZnO NRs on the Au tips. The lattice fringes of 0.260 nm belong to the (0001) plane of wurtzite-type ZnO and the Au tips are terminated by the (111) plane with a *d*-spacing of 0.235 nm. Without adding a non-polar solvent, 1-octadecene, Au–ZnO NRs with bi-, tri-, or tetrapod shapes were obtained in a polar solvent of benzyl alcohol. In addition, Au–ZnO core–shell nanoparticles were formed by using dodecanol, a more polar solvent, in our previous work.[15] According to our synthesis experimental results, a possible growth mechanism of matchstick-shaped Au–ZnO NRs can be

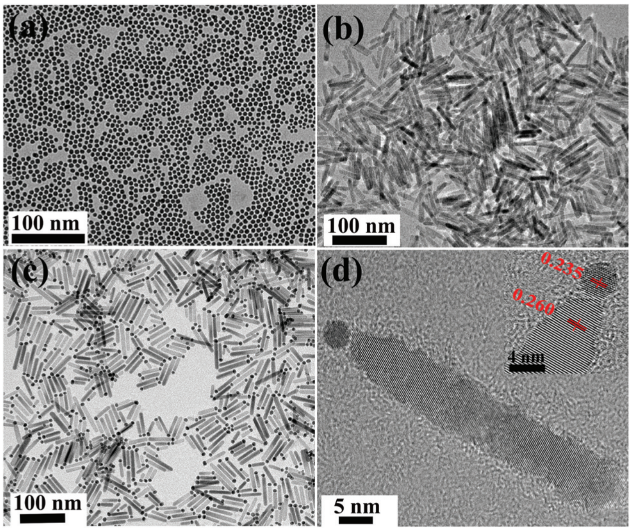

Fig. 1 TEM images of (a) Au seeds, (b) ZnO NRs, (c) Au–ZnO NRs, and (d) HRTEM images of branched Au–ZnO NRs.

deduced. To our knowledge, the lower energy barrier favors the heterogeneous nucleation of semiconductor nanostructures onto the metal seeds. The hexagonal basal surface of ZnO is the (0001) polar plane. Because of the lower interface energy for the polar/metal interface, the ZnO (0001) is favourable to nucleate on the Au (111) plane. During the growth process, the free electrons from the Au seeds will compensate for the charge induced by the polarized plane at the Au–ZnO interface. As the electron concentration within a single Au seed is limited, this compensation makes all other facets of the Au seeds more electron deficient and therefore less reactive for adding other nuclei. As a result, linear ZnO nanostructures are formed.[16] When solvents with a higher polarity are used, the Au seeds can compensate for the reduced electron density by polarization due to the solvent, which allows nucleation on multiple facets.

The crystal structures and interfaces of the matchstick-shaped Au–ZnO NRs were further analysed by aberration-corrected STEM. Figs. 2a and b show the annular bright field (ABF) and high-angle annular dark field (HAADF) STEM images of the Au–ZnO NRs, respectively. The clear spatial configurations of the Au tip, ZnO nanorod, and interface can be observed, respectively. The corresponding FFTs acquired from the selected Au and ZnO domains shown by the red square indicate that the ZnO NRs grow along the direction of ⟨0001⟩ of ZnO after nucleation on the Au (111) planes. From the enlarged ABF and HAADF images of the interface of Au–ZnO NRs (as shown in Fig. 2c and d), the ZnO NRs grow well epitaxially on the synthesized Au tips and both the Au tips and ZnO NRs keep their own crystal structures well at the interface. The interface is also free of any significant voids or defects. These characteristics suggest that almost no other energy barriers are introduced across the interface. It is known that the contrast of ABF and HAADF images directly depends on the atomic number, Z ($\sim Z^{1.7}$ dependence), which could be used to identify the positions of the heavier Au and Zn atoms. ABF is sensitive to both heavy and light elements, with heavier elements showing a darker contrast. Careful analysis of the simultaneously acquired STEM-ABF and HAADF images (Fig. 2c and d) reveals that the ZnO/Au interface is terminated by the Zn atomic plane. A schematic structural model of the interface is overlaid on the images, with Au, Zn, and O atoms shown in golden, gray, and red colors, respectively.

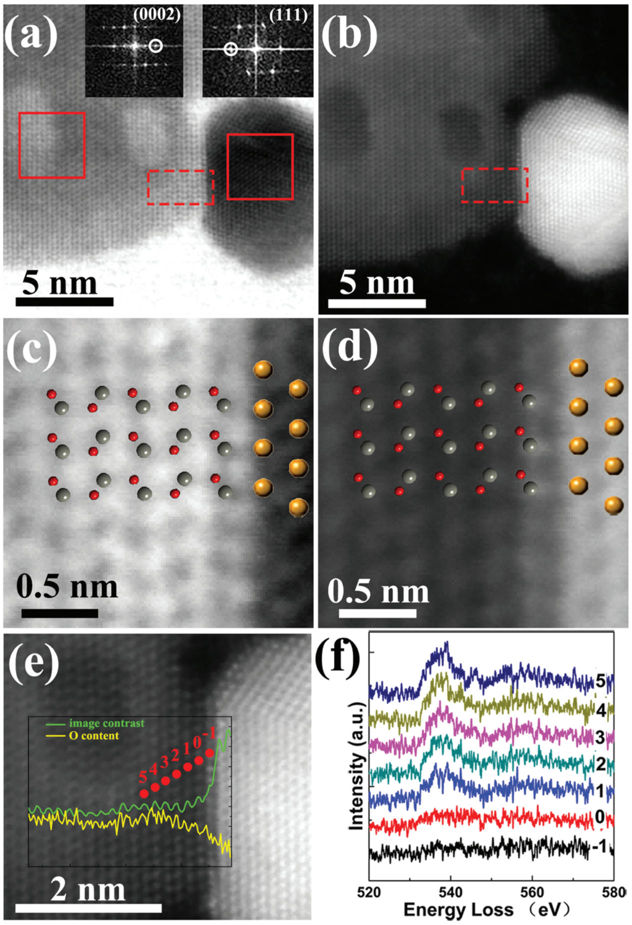

Fig. 2 (a) The annular bright field (ABF) STEM image and (b) high-angle annular dark field (HAADF) STEM image of the Au–ZnO NRs; the insets are the FFT patterns of the selected area shown by red lines; (c) and (d) are the corresponding enlarged interface parts shown by red dotted lines in (a) and (b), the simulated structures of Au and ZnO atoms are shown; (e) HAADF-STEM image of Au–ZnO NRs for showing the atom columns used to collect the atomic-column resolution EELS spectra *via* the line-scan mode; the insets show the corresponding image contrast and oxygen content. (f) Corresponding EELS spectra of the 7 atom columns of oxygen cations scanned along the dotted red line in (e).

To reveal the combining state of the interfacial atoms of the metal–semiconductor, which has a strong influence on the transport or scattering properties of plasma-induced hot electrons, atomic-column resolution EELS spectra in the line-scan mode were obtained. In the HAADF image in Fig. 2e, numbers 1–5 correspond to the scanned seven atomic columns across the interface along the red line. The contrast intensity profile of the atomic columns indicates that atomic columns 0 and −1 have a higher contrast than that of atomic columns 1–5, while much less than that of the inner Au atoms. The corresponding EELS spectra of O ions (K edge, 532 eV) with the background subtracted using a power law are shown in Fig. 2f. No absorption peak of the K edge is observed in the spectra of atomic columns −1 and 0, which indicates that they are Au and Zn columns. Moreover, there is no obvious chemical shift in the absorption peaks of the K edge in the observed spectra of atomic columns 1–5, which reveals that Au atoms do not form Au–O bonding or have little influence on the O ions even in the neighbouring O polar plane. This is quite different from the Au–O bonding observed in the Au–Fe_3O_4 core–shell nanoparticles.[17] Thus, it can be concluded that the Au–Zn–O atomic layer stack exists in the interfaces of the matchstick-shaped Au–ZnO NRs with a strong electronic affinity between the Au atom and Zn^{2+} ions, which benefits electronic transport from metals to semiconductors.[18]

To investigate the SERS of Au–ZnO NRs, the dopamine molecule is used since it has a phenyl ring with a large polarization degree and polar molecular groups, which allows dopamine to tightly bind to the surface of ZnO with a large CT response. UV-vis absorption spectra were obtained to determine the suitable radiation wavelength for Raman measurements and confirm the dopamine binding with ZnO NRs. Fig. 3 shows the UV-vis absorption spectra of the Au seeds, ZnO NRs, and Au–ZnO NRs before and after absorbing dopamine molecules, respectively. The absorption spectra of Au seeds exhibit an absorption band with a maximum absorption wavelength ($\lambda_{\max}$) of about 520 nm, which is caused by the localized surface plasmon resonance (LSPR) of gold seeds. An absorption band with a maximum absorption wavelength ($\lambda_{\max}$) is located at 358 nm due to the ground excitonic state of ZnO. After combining with ZnO NRs, the characteristic gold plasma resonance peak (Fig. 3c) red-shifts from 520 nm to 556 nm against pure Au seeds because the dielectric functions of semiconductors are larger than those of water, air, or organic capping molecules based on the Mie theory.[19] It can also be found that after adsorbing the dopamine molecules (Fig. 3d), the absorption band at 364 nm shifts to 359 nm. These changes are attributed to the electronic interaction of dopamine molecules and ZnO NRs. Meanwhile, besides the LSPR absorption band of ZnO NRs, the absorption band of Au seeds shows a blue shift from 556 nm to 552 nm, which means that a variation in dielectric surroundings can change the LSPR behaviour of Au–ZnO NRs.

Fig. 4 shows the Raman spectra of dopamine molecules adsorbed on the different nanostructures at a laser excitation wavelength of 532 nm. The predominant bands in the spectrum of 2 M dopamine solution (as shown in Fig. S2†) are located at 753, 792, 1113, 1294, 1147, 1454, and 1602 cm^{-1} corresponding to the C–O, CH_2, and phenyl ring stretching modes.[20] For dopamine with 10^{-5} M concentration, no Raman peak is observed (Fig. 4a) except for a rectangle-shaped peak corresponding to the Si substrate at 938 cm^{-1}. In the case of ZnO NRs, there is a slightly broad peak at 1600 cm^{-1}, indicating a weak CT enhancement effect of ZnO. Au seeds, as typical SERS substrates with the EM enhanced mechanism, show a strong Raman peak at 1583 cm^{-1} corresponding to the C–C stretching in the phenyl ring. Strong bands are observed at 790, 1092, 1363, 1583, 1765, and 1904 cm^{-1} in the Au–ZnO NR absorbed dopamine molecules in Fig. 4d, corresponding to the C–C bending modes, OH-C bending modes, C–O stretching, and C–C stretching modes, respectively. Five Raman peaks of the dopamine molecules experienced different relative enhancements, especially the intensity at 1583 cm^{-1} is obviously much higher than that in the other bands. For dopamine with a concentration level of 10^{-5} M, the enhancement factor of Au–ZnO NRs is over 1.2×10^4. It means that the vibrational modes of dopamine molecules are selectively enhanced on the surface of ZnO NRs. C–C bonding in the phenyl ring with a high molecular polarity is subject to enhancement by the CT effect of a semiconductor. By comparing curves c and d in Fig. 4, the peak intensity of Au–ZnO NRs at 1583 cm^{-1} increases to twice that of Au seeds. Thus, it is reasonable to conclude that these strong SERS signals are the result of the chemical enhancement mechanism because there is no resonant excitation of plasmons in ZnO NRs. The CT enhancement effect can further be improved by transferring the additional electrons from the LSPR of Au tips to the conduction band of the ZnO NRs. Subsequently, dynamic CT could occur through coupling with the vibrations of the bridging molecules to easily transfer an electron to an excited unfilled level of dopamine. The enhanced CT effect has also been proved by a higher photocatalysis efficiency of Au–ZnO NRs than pure Au seeds, as shown in Fig. S4.†

In order to further reveal the mechanism of enhanced Raman spectra of label molecules on the Au–ZnO NRs, the SERS of dopamine molecules was measured using 532 nm, 633 nm, and 785 nm radiation as the excitation sources, respectively (as shown in Fig. 5). Using the 633 nm excitation source, only two obvious weak broad Raman peaks at 1330 cm^{-1} and 1584 cm^{-1} are observed. The SERS spectrum using 785 nm laser excitation only has a sharp asymmetric peak with a lower intensity corresponding to the Si substrate at 938 cm^{-1}. These can be attributed to the low LSPR intensity of

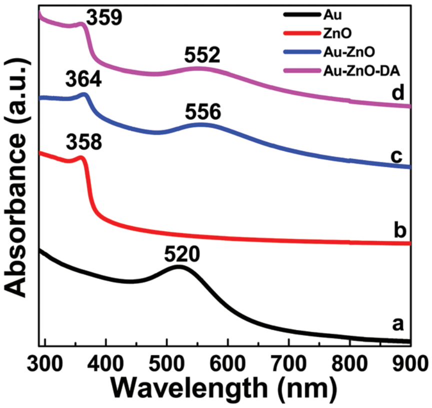

Fig. 3 UV-vis absorption spectra of (a) Au seeds, (b) ZnO NRs, (c) Au–ZnO NRs, and (d) Au–ZnO NRs after absorbing dopamine.

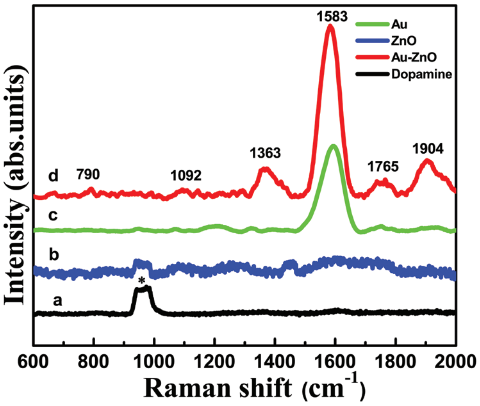

Fig. 4 SERS spectra of (a) dopamine molecules with a concentration of 10^{-5} M and its adsorption with (b) ZnO NRs, (c) Au seeds, and (d) Au–ZnO NRs with 532 nm laser excitation. The broad peak marked by the star (*) is from Si.

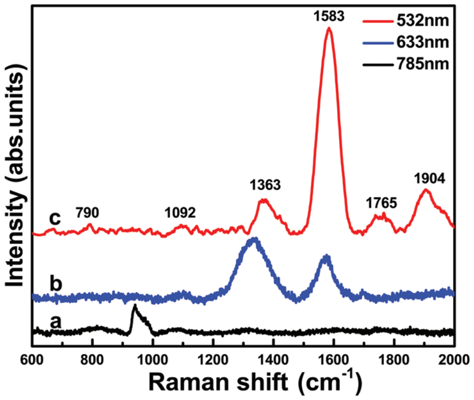

Fig. 5 SERS spectra of dopamine molecules adsorbed on the Au–ZnO NRs under (a) 532 nm excitation, (b) 633 nm excitation, and (c) 785 nm excitation. The broad peak marked by the star (*) is from Si.

Au tips excited under some excitation sources at a wavelength far from the 520 nm of the Au plasmon band, which cannot strongly accelerate the CT enhancement effects of ZnO NRs.

We next investigate the mechanisms of exciton and plasmon interactions in the Au–ZnO heterogeneous NRs. Pump–probe transient absorption spectroscopy was used to probe the dynamics of excited states in the metal domains. The setups of femtosecond mid-IR transient absorption are described in the ESI.† In the transient absorption experiments, Au seeds, ZnO NRs, and their physical mixtures are used as reference samples to compare with the dynamics observed in Au–ZnO NRs. The reference samples have the same concentration as that of the Au–ZnO samples. Under these conditions, the reference samples and the Au–ZnO NRs samples absorb the same number of excitation photons. The samples for transient absorption studies were excited by 360 and 520 nm laser pulses and probed at 3800 nm corresponding to the intraband absorption of ZnO.[21,22] Fig. 6a and b show the kinetics of all samples after 360 and 520 nm laser pulse excitation. With 360 nm excitation, all samples except for Au seeds generate an intraband absorption signal at 3800 nm, as shown in Fig. 6a, which shows a multiexponential decay. Though Au seeds may be excited by a 360 nm beam, no transient absorption features can be observed at 3800 nm due to no intraband absorption in the mid-IR region in Au seeds. The traces in Fig. 6a can be fit with a rise time of 0.058 ± 0.004 ps, 0.064 ± 0.003 ps, and 0.083 ± 0.010 ps for ZnO NRs, mixtures, and Au–ZnO NRs, respectively. A slightly slower rise time of Au–ZnO NRs may be caused by partial electron transfer from the weak LSPR of Au tips to ZnO NRs. After 520 nm excitation, only Au–ZnO NRs have been excited and generate an intraband absorption signal at 3800 nm along with a multiexponential decay in 100 ps, as shown in Fig. 6b. No intraband absorption signal can be observed in ZnO NRs and Au seeds because isolated ZnO NRs cannot be excited by a 520 nm beam and Au seeds cannot be probed at 3800 nm after 520 nm beam excitation. Meanwhile, the mixture of isolated Au seeds and ZnO NRs coated by surfactant molecules has no effective electron transfer pathway between them, resulting in no obvious excitation. The kinetics of Au–ZnO NRs can be fitted with a rise time of 0.720 ± 0.120 ps. Fig. 6c shows the kinetics comparison for the transient signals of Au–ZnO NRs with different excitation wavelengths of 360 and 520 nm in a short timescale. A much slower rising time of 0.720 ps under the 520 nm laser pulse excitation than 0.083 ps under 360 nm pulse excitation can obviously be observed. Lian *et al.* reported that the rise times in Au–CdSe and Au–CdS NRs with the 1.74 and 2.49 eV band gaps of semiconductor NRs are 0.020 ps and 0.090 ps, respectively, after 590 nm beam excitation.[11,23] The much faster rise time in Au–CdSe NRs is ascribed to the PICTT mechanism, while the slower rising time of 0.090 ps in Au–CdS NRs cannot

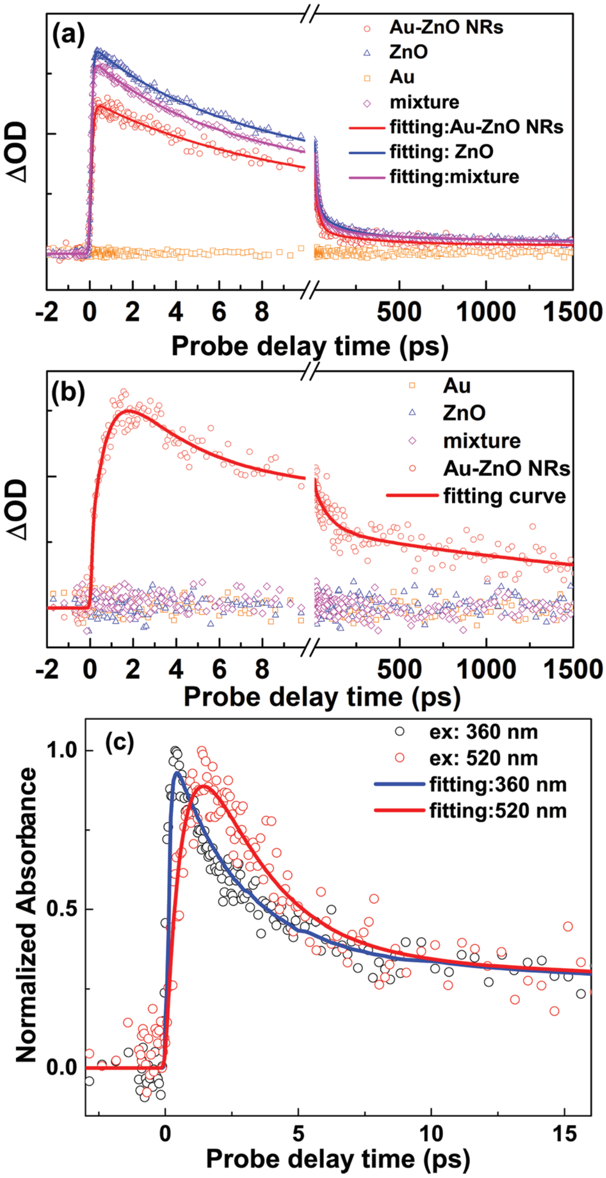

Fig. 6 TA kinetics of different samples after (a) 360 and (b) 520 nm excitation. Kinetics probed at 3800 nm for all samples. The solid line is a multiexponential fit to the kinetics of all samples. (c) The enlarged TA kinetics of Au–ZnO NRs after 360 and 520 nm excitation.

be ascribed to the PICTT mechanism. Meanwhile, the conventional indirect electron-transfer model suggests that the timescale of the PHET process should be on the order of picoseconds.[24] Based on the 0.720 ps rising time, it can be reasonably concluded that the transfer of the plasmon-induced electron is an indirect pathway processing two steps including the decay of plasmons and the transfer of hot electrons from the interface of Au–ZnO to the CB of ZnO. However, a fine Au–Zn–ZnO interface with a low Schottky barrier in the Au–ZnO NRs can accelerate the transfer of hot electrons after plasmon decay, which results in a shorter rising time less than 1 ps. Another important dynamic characteristic is that the decay time under 360 nm laser pulse excitation is 2.41 ± 0.70 ps referring to the charge-recombination time in ZnO NRs. The decay time under 520 nm pulse excitation is 3.63 ± 0.67 ps corresponding to the inverted electron transfer process through the Au–ZnO interface from the ZnO NRs to Au tips, which can occur *via* the dense manifold of unfilled conduction band levels above the Fermi level of Au tips. Such long recombination kinetics of injected hot electrons can greatly increase the transfer ratio of electrons from ZnO to the absorbed molecules, which results in not only an enhanced SERS effect but also excellent photocatalysis properties for the fast photodegradation of 4-chlorophenol.

Based on these results, the PHET mechanism for Au–ZnO NRs and the PICTT mechanism for Au–CdSe NRs can be reasonably illustrated in Fig. S5.† The plasmon excitation decays to hot electrons and holes due to Landau damping, in which a plasmon quantum is transferred into an intraband excitation within the conduction band of the metal or an interband excitation between occupied bands (usually d bands) and the conduction band. There are earlier results reported by Y. K. Lee *et al.* on the direct observation of plasmon-induced hot electron flows by using metal–semiconductor Schottky structures.[25,26] When plasmonic nanostructures are usually smaller than 20 nm, intraband transitions take place due to nano-confinement effects and alter the hot carrier distributions with electrons at lower plasmon energies by directly exciting electrons from the Fermi level of plasmonic nanostructures.[27] Since the Schottky barrier of Au–CdSe NRs is only 0.6 eV and the Fermi level of Au is very close to the valence band of CdSe, the decay of Au plasmons could directly excite an electron in the conduction band of the CdSe and a hole in the Au due to the strong coupling and mixing between Au and CdSe energy levels and a narrow barrier layer. However, the Schottky barrier of Au–ZnO is as high as 1.2 eV and the difference between the valence band of ZnO and the Fermi level of Au is 0.8 eV, which results in a wide barrier layer and poor mixing between Au and CdSe energy levels. It should be noted that the Schottky barrier of the nanoscale Schottky junction typically is dozens of meV lower than the bulk values.[28,29] Only hot electrons with high energy can transfer to the conduction band of ZnO, and the direct tunnelling of plasmon-induced hot electrons from the Au to ZnO even with a fine interface between them becomes very difficult. Thus, we propose that the PICTT mechanism may exist in the metal–semiconductor system with a perfect mixing of the metal and semiconductor band levels, especially consisting of a narrow band gap semiconductor and plasmatic metal nanostructures with the corresponding plasma absorption wavelength. While for the metal–semiconductor system with a large energy level difference between the metal and semiconductor band levels, the PHET mechanism would come into play in the plasmon-induced hot-electron injection.

Conclusions

In summary, matchstick-shaped Au–ZnO nanorods have been prepared *via* a facile one-pot colloid synthesis method. The Zn ion terminated plane in the ZnO–Au interface without the formation of Au–O bonds is found based on the atomic-resolution observation of their interfacial structure and electronic states, which is greatly different from widely-reported results. The Au–ZnO NRs as SERS substrates for detection of DA molecules have shown a stronger SERS signal than Au seeds when using 532 nm laser excitation. The obvious SERS enhancement in the number and amplitude of the Raman peaks of the DA molecules absorbed on the Au–ZnO NRs reveals that the CT effect of ZnO is greatly enhanced by the LSPR of Au seeds. Furthermore, the LSPR-enhanced CT effect has been proven from the SERS spectra of DA molecules excited at different laser wavelengths from 325 to 785 nm. Moreover, the photocatalytic experimental results showed that Au–ZnO NRs are characterized by high reproducibility after visible-light-assisted cleaning, which makes them promising as biologically compatible and recyclable SERS-active platforms for different molecular species. The PHET mechanism in Au–ZnO heterogeneous NRs has been confirmed by transient absorption spectroscopy. These findings suggest the dependency of the plasmon-induced hot electron injection mechanism on the different types of mixing of the metal and semiconductor band levels.

Conflicts of interest

There are no conflicts to declare.

Acknowledgements

This work was supported by the National Nature Science Foundation of China (Grant No. 11274370, 51471185, 21633015, and 11721404) and the National National Key R&D Program of China (Grant No. 2016YFJC020013, 2018FYA0305800, and 2018YFA0208701).

Notes and references

1 C. Clavero, *Nat. Photonics*, 2014, **8**, 95.
2 H. Robatjazi, H. Zhao, D. F. Swearer, N. J. Hogan, L. Zhou, A. Alabastri, M. J. McClain, P. Nordlander and N. J. Halas, *Nat. Commun.*, 2017, **8**, 1.

3 J. T. Zhang, Y. Tang, K. Lee and M. Ouyang, *Nature*, 2010, **466**, 91.
4 J. F. Li, Y. J. Zhang, S. Y. Ding, R. Panneerselvam and Z. Q. Tian, *Chem. Rev.*, 2017, **117**, 5002.
5 Z. Li, Y. N. Gao, L. S. Zhang, Y. Fang and P. J. Wang, *Nanoscale*, 2018, **10**, 18720.
6 E. D. Feng, T. T. Zheng, X. X. He, J. Q. Chen and Y. Tian, *Sci. Adv.*, 2018, **4**, eaau3494.
7 A. Musumeci, D. Gosztola, T. Schiller, N. M. Dimitrijevic, V. Mujica, D. Martin and T. Rajh, *J. Am. Chem. Soc.*, 2009, **131**, 6040.
8 J. R. Lombardi and R. L. Birke, *J. Phys. Chem. C*, 2014, **118**, 11120.
9 G. V. Hartland, *Chem. Rev.*, 2011, **111**, 3858.
10 C. Boerigter, U. Aslam and S. Linic, *ACS Nano*, 2016, **10**, 6108.
11 K. Wu, J. Chen, J. R. McBride and T. Lian, *Science*, 2015, **349**, 632.
12 V. G. Rao, U. Aslam and S. Linic, *J. Am. Chem. Soc.*, 2019, **141**, 643.
13 Z. H. Chen, Y. B. Tang, C. P. Liu, Y. H. Leung, G. D. Yuan, L. M. Chen, Y. Q. Wang, I. Bello, J. A. Zapien, W. J. Zhang, C. S. Lee and S. T. Lee, *J. Phys. Chem. C*, 2009, **113**(30), 13433.
14 B. J. Coppaa, R. F. Davis and R. J. Nemanich, *Appl. Phys. Lett.*, 2003, **82**, 400.
15 L. P. Liu, H. T. Yang, X. Ren, J. Tang, Y. F. Li, X. Q. Zhang and Z. H. Cheng, *Nanoscale*, 2015, **7**, 5147.
16 L. Wu, A. Mendoza-Garcia, Q. Li and S. Sun, *Chem. Rev.*, 2016, **116**, 10473.
17 L. Zhu, X. Deng, Y. Hu, J. Liu, H. B. Ma, J. L. Zhang, J. Fu, S. S. He, J. Wang, B. D. Wang, D. S. Xue and Y. Peng, *Nanoscale*, 2018, **10**, 21499.
18 B. Y. Zheng, H. Zhao, A. Manjavacas, M. McClain, P. Nordlander and N. J. Halas, *Nat. Commun.*, 2015, **6**, 7797.
19 A. C. Templeton, J. J. Pietron, R. W. Murray and P. Mulvaney, *J. Phys. Chem. B*, 2000, **104**, 564.
20 W. Song, X. X. Han, L. Chen, Y. M. Yang, B. Tang, W. Ji, W. D. Ruan, W. Q. Xu, B. Zhao and Y. Ozaki, *J. Raman Spectrosc.*, 2010, **41**, 907–913.
21 M. Shim and P. Guyot-Sionnest, *Phys. Rev. B: Condens. Matter Mater. Phys.*, 2001, **64**, 245342.
22 M. Shim and P. Guyot-Sionnest, *J. Am. Chem. Soc.*, 2001, **123**, 11651.
23 K. F. Wu, W. E. Rodríguez-Cordoba, Y. Yang and T. Q. Lian, *Nano Lett.*, 2013, **13**, 5255.
24 P. Christopher and M. Moskovits, *Annu. Rev. Phys. Chem.*, 2017, **68**, 379.
25 Y. K. Lee, C. H. Jung, J. Y. Park, H. Seo, G. A. Somorjai and J. Y. Park, *Nano Lett.*, 2011, **11**, 4251.
26 H. Lee, H. Lee and J. Y. Park, *Nano Lett.*, 2019, **19**, 891.
27 R. Sundararaman, P. Narang, A. S. Jermyn, W. A. Goddard III and H. A. Atwater, *Nat. Commun.*, 2014, **5**, 5788.
28 V. Subramanian, E. E. Wolf and P. V. Kamat, *J. Am. Chem. Soc.*, 2004, **126**, 4943.
29 M. Asghar, K. Mahmood, S. Rabia, B. M. Samaa, M. Y. Shahid and M. A. Hasan, *IOP Conf. Ser.: Mater. Sci. Eng.*, 2014, **60**, 012041.